# Modeling Spin-Precessing Neutron Star Binaries: A Generalization of Black Hole Binary Frameworks in `Precession`
# 2026 LIGO SURF Proposal

Quinn Kasdan-Grollo, Giulia Fumagalli, and Taylor Knapp
(Dated: July 31, 2026)

## I. INTRODUCTION

The LIGO/Virgo/KAGRA (LVK) collaboration's observational focus falls on massive compact binaries – binaries with black holes (BHs) and neutron stars (NSs). In these massive, relativistic systems the two object's spin introduces interactions between spins and the orbital angular momentum of the binary. The resulting motion from these spin-spin and spin-orbit couplings is precession and nutation of the orbital plane and spin vectors, respectively [1–3]. Gerosa *et al.* introduced a multi-timescale analysis to precession-average the evolution of binary black holes (BBHs), which has been used to better understand different spin morphologies and formation channels of BBHs. Left unresolved is the NS case. In this project we extend the work on precessing BBHs to NSs, opening up opportunities to investigate binary neutron star (BNS) spin morphologies, their relation to BNS formation channels, and NS equations of state (EOSs).

The precession averaged equations developed in [4] are written at second post-Newtonian order (2PN), where the spin-induced quadrupole moment, $Q = -k\chi^2 M^3$, affects the evolution of the spin and orbital angular momentum. Here $k$ is a scalar quantity related to the object's tidal deformability, $\chi$ is the dimensionless kerr parameter of the object (related to its spin), and $M$ is the mass of the object. Due to the no-hair theorem, BHs have $k = 1$. Meanwhile, the EOS of NSs is unconstrained and so their value of $k$ is unknown. This requires generalizing the precession-averaged equations in [4] to binaries with $k > 1$. Doing so results in $\chi_{\rm eff}$ – the effective spin of the binary – no longer being constant on the precessional timescale. Thus, we introduce a new parameter, $\chi_{\rm cons}$ that remains constant on the precessional timescale, allowing us to precession average. This re-parameterization makes finding the bounds of the precessional cone to average over non-analytical, slower, and not always successful. We solve this problem by recognizing helpful bounds on the equation which describes precession, and optimize our calculations to allow for investigation of precessing BNSs. In some cases, though, two physical precession cones – where the objects' spins oscillate between – are formed during inspiral. This arises due to the loss of phase information from precession-averaging. We hope to understand the conditions from which this arises, and believe that this behavior encodes valuable information about the existence, or non-existence, of NSs with high tidal deformability.

## II. BACKGROUND

### A. Gravitational Waves and Compact Binary Coalescence

Gravitational waves (GWs), as predicted by Albert Einstein's theory of General Relativity, are ripples in space-time produced by massive objects accelerating through the fabric of spacetime [5]. The faster and more massive the object, the more pronounced the ripples – analogous to a motorboat creating larger waves than a duck moving across a pond. GWs, though, are quite hard to detect, despite distorting spacetime they have no noticeable effect on Earth. Thus, to detect GWs we focus our attention to the most massive and relativistic sources – compact binaries and compact binary coalescence. Compact binaries are binary systems consisting of BHs and/or NSs. Initially, the compact objects orbit each other at high speeds, emitting weak GWs that reduce the total angular momentum and orbital energy of the system. Due to this loss of angular momentum and energy, their orbital separation decreases as their orbital velocities increase, eventually initiating an inspiral and merger. In Figure 1 the evolution of a compact binary is shown compared to the predicted strain on a detector. For this project we will focus our attention on the inspiral phase as that is where the key 2PN approximations used can safely be applied.

### B. Spin-Induced Precession

Compact objects can spin which, as predicted by General Relativity, drags the space-time around them. In binary systems, this space-time dragging can affect the orbit and spin of the system through spin-orbit and spin-spin couplings. Let the spin vectors of compact objects 1 and 2 be $\mathbf{S_1}$ and $\mathbf{S_2}$, respectively, and the system's total spin, $\mathbf{S}$, be defined as $\mathbf{S} = \mathbf{S_1} + \mathbf{S_2}$. When $\mathbf{S}$ is misaligned with $\mathbf{L}$ the system will precess. That is, if $\mathbf{S}$ is not parallel or anti-parallel to $\mathbf{L}$, precession occurs. This precession occurs about the systems total angular momentum vector, $\mathbf{J}$, defined as $\mathbf{J} = \mathbf{S} + \mathbf{L}$. A useful graphic showing these vectors and how $\mathbf{L}$ precesses about $\mathbf{J}$ can be found in Figure 2. In summary, due to spin-orbit vector misalignment, precession occurs.

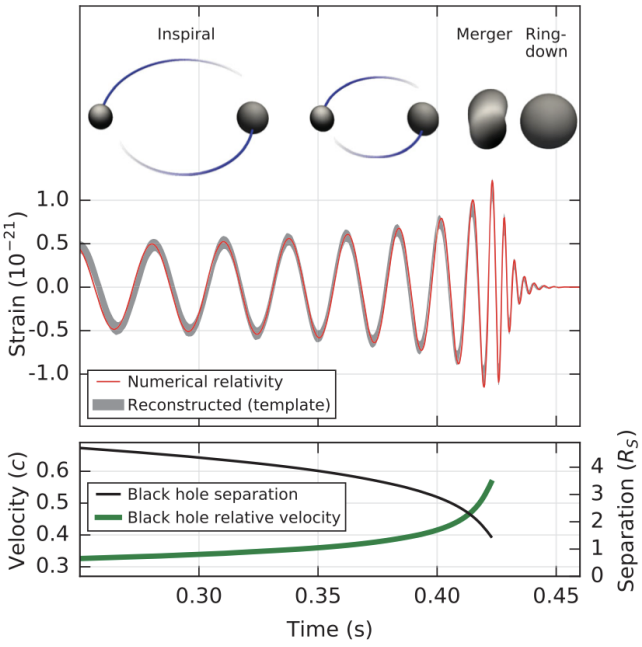



FIG. 1. The predicted strain detected by LIGO from GW150914 – the first detected GW – over inspiral to merger to ring-down as a function of time. Also displayed is the velocity ($v/c$) compared to the orbital separation [6].

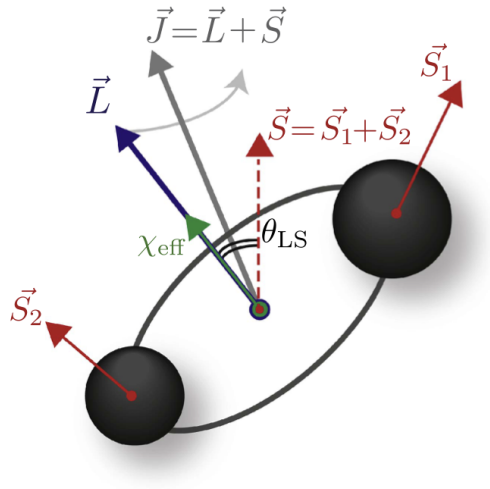



FIG. 2. From Ref. [7] this graphic gives a clear look at the different angular momentum vectors in a spinning binary system as described in Section II B along with $\chi_{\rm eff}$ and $\theta_{LS}$ – the effective spin and the spin-orbit misalignment angle, respectively.

### C. The Timescale Hierarchy

At 2PN, the treatment of precessing compact binaries admits a timescale hierarchy which greatly simplifies the problem at hand: the orbital motion takes place on $t_{\rm orb} \propto (r/M)^{3/2}$ while the spins precess on $t_{\rm pre} \propto (r/M)^{5/2}$ [8]. That is, for sufficiently large separations, $t_{\rm orb} \ll t_{\rm pre}$ – multiple orbits occur before precession of the spins and orbital plane changes their orientation significantly. With this in mind, Ref. [1] employs the oft-used method of "orbit averaging", to describe the change in spin and orbital angular momentum throughout inspiral. This useful technique allows for the study of the effects of precession on the detected waveform of binaries, as Apostolatos *et al.* thoroughly investigates.

To study compact binary dynamics from formation to merger though, the purely orbit-averaged approach requires tracking the orientations of spin and momentum vectors at each time step during integration – as one can imagine, storing all this information adds up quickly, making orbit averaging quite slow. Thankfully, Gerosa *et al.* derive a way to simplify the orbit-averaged spin and momentum evolutions. Then, by recognizing that $t_{\rm RR} \propto (r/M)^4$ – the timescale at which the orbital separation shrinks significantly – they complete the timescale hierarchy (for $r > 10$),

$$t_{\rm orb} \ll t_{\rm pre} \ll t_{\rm RR}. \tag{1}$$

Just as orbit-averaging relied on $t_{\rm orb} \ll t_{\rm pre}$, the right hand side, $t_{\rm pre} \ll t_{\rm RR}$ opens up the opportunity for "precession averaging". Ref. [4] uses their simplified precession descriptions to find bounds for which the spin and angular momentum vectors oscillate between, over $t_{\rm pre}$. At the cost of storing the exact orientation of spin and momentum vectors across the entire time of evolution, Ref. [4] developed a way to understand the evolution of the "shape" of precession throughout a binary's evolution extremely efficiently. Most of this has been a hand-wavy description of precession averaging and the relevant quantities actually tracked, we present formalized definitions of relevant information more formally in Sections II E and II F. For now, it is important to understand that the basis of our work relies on precession averaging, which is used to make evolving compact binaries faster than the commonly used orbit averaging.

### D. Physical Setup in a Co-Precessing Frame

Following the set up in Ref. [8], we consider a compact binary with masses $m_1 \geq m_2$. The total mass $M = m_1 + m_2$ does not affect the shape of the problem, only the scale, thus we set it to $M = 1$ in our implementation. The mass ratio is defined as $q = m_2/m_1 \in (0, 1]$ and the Kerr parameters as $\chi_{1,2} = S_i/m_i^2 \in [0, 1]$. The spin magnitudes are given as:

$$S_1 = \frac{\chi_1}{(1+q)^2} M^2 \,, \tag{2}$$

$$S_2 = \frac{q^2 \chi_2}{(1+q)^2} M^2 \,. \tag{3}$$

In this project we restrict our focus to quasi-circular orbits, leaving the orbital angular momentum to be expressed as

$$L = M^2 \frac{q}{(1+q)^2} \sqrt{\frac{r}{M}}\,, \tag{4}$$

and the compactified coordinate (helpful for calculations) as

$$u = \frac{1}{2L}\,, \tag{5}$$

where $u \to 0$ as $r \to \infty$.

In a co-precessing frame, we fix the $\hat{z}$-axis to $\mathbf{L}$ and are able to describe the orientations of our spin and momentum vectors with three angles, the angles between the spins and orbital angular momentum, $\theta_{1,2} \in [0, \pi]$ and the azimuthal angle $\Delta\Phi \in [-\pi, \pi]$ between the projections of the spins onto the plane. These are defined by,

$$\cos\theta_1 = \hat{\mathbf{S}}_\mathbf{1} \cdot \hat{\mathbf{L}}, \tag{6}$$

$$\cos\theta_2 = \hat{\mathbf{S}}_\mathbf{2} \cdot \hat{\mathbf{L}}, \tag{7}$$

and

$$\cos\Delta\Phi = \frac{\hat{\mathbf{S}}_\mathbf{1} \times \hat{\mathbf{L}}}{|\hat{\mathbf{S}}_\mathbf{1} \times \hat{\mathbf{L}}|} \cdot \frac{\hat{\mathbf{S}}_\mathbf{2} \times \hat{\mathbf{L}}}{|\hat{\mathbf{S}}_\mathbf{2} \times \hat{\mathbf{L}}|}, \tag{8}$$

$$\mathrm{sgn}\Delta\Phi = \mathrm{sgn}\{\mathbf{L} \cdot [(\mathbf{S}_1 \times \mathbf{L}) \times (\mathbf{S}_2 \times \mathbf{L})]\}. \tag{9}$$

With these definitions we fully capture the orientations and magnitudes of our quantities of interest. Figure 3 shows these vectors and angles clearly.

### E. Constants of motion & spin evolution dynamics

To understand the usefulness of precession averaging, we present the 2PN orbit-averaged equations Gerosa *et al.* uses to continue onto precession averaging, then we shall compare them with the 9-dimensional equations that one gets before reparameterization.

To capture the spin dynamics and evolution succinctly, we define

$$\chi_{\rm eff} \equiv \frac{(1+q)}{M^2}\left(\mathbf{S}_1 \cdot \hat{\mathbf{L}} + \frac{\mathbf{S}_2 \cdot \hat{\mathbf{L}}}{q}\right) = \frac{\chi_1 \cos\theta_1 + q\chi_2 \cos\theta_2}{1+q} \tag{10}$$

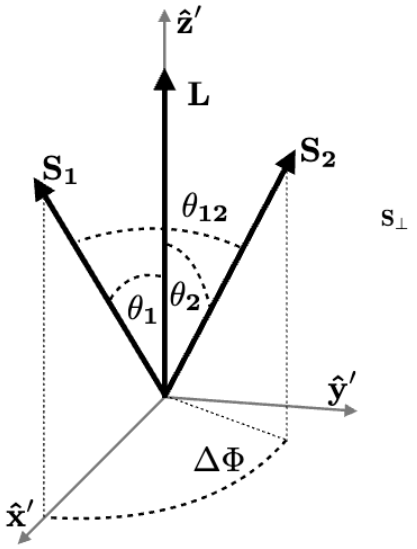



FIG. 3. A depiction of the co-precessing we use, the spins and orbital angular momentum, and angles described by Equations (6) - (8)

and

$$\delta\chi \equiv \frac{(1+q)}{M^2}\left(\mathbf{S}_1 \cdot \hat{\mathbf{L}} - \frac{\mathbf{S}_2 \cdot \hat{\mathbf{L}}}{q}\right) = \frac{\chi_1 \cos\theta_1 - q\chi_2 \cos\theta_2}{1+q}\,. \tag{11}$$

$\chi_{\rm eff}$ may be familiar to many in the LVK collaboration, it is the spin quantity commonly measured by LVK observations. For our purposes, $\chi_{\rm eff}$ is of interest as it is conserved on $t_{\rm pre}$ for BBHs (when $r$ is kept constant) [3]. $\delta\chi$ is less commonly recognized, we refer to this as the "weighted spin-difference" [9].

Also constant on $t_{\rm pre}$ is $J$ and $L$ since $L \propto r^{1/2}$ and $S_{1,2}$ do not vary with $r$ (Equations 2 - 4), thus $J$ too only varies with changing $L$. So, $J$ remains constant if $r$ is held constant. We introduce the "asymptotic angular momentum",

$$\kappa = \frac{J^2 - L^2}{2L}\,, \tag{12}$$

which clearly is constant on $t_{\rm pre}$. This is done since $J$ diverges as $r \to \infty$ [10]. $\delta\chi$, $\chi_{\rm eff}$, and $\kappa$ paired together are nice as they carry all interesting information about our compact binary, but only $\delta\chi$ varies on $t_{\rm pre}$. Without this re-parameterization we are left solving a 9-dimensional problem defined by,

$$\frac{d\boldsymbol{S}_1}{dt} = \frac{1}{2r^3}[\mathcal{S}_1\boldsymbol{L} + \boldsymbol{S}_2] \times \boldsymbol{S}_1, \tag{13}$$

$$\frac{d\boldsymbol{S}_2}{dt} = \frac{1}{2r^3}[\mathcal{S}_2\boldsymbol{L} + \boldsymbol{S}_1] \times \boldsymbol{S}_2 \tag{14}$$

$$\frac{d\boldsymbol{L}}{dt} = \frac{1}{2r^3}[\mathcal{S}_1\boldsymbol{S}_1 + \mathcal{S}_2\boldsymbol{S}_2] \times \boldsymbol{L} + \frac{dL}{dt}\hat{\boldsymbol{L}} \tag{15}$$

where,

$$\mathcal{S}_1 = 4 + 3q - \frac{3(1+q)^2}{\sqrt{r/M}}(k_1\boldsymbol{S}_1 + \frac{\boldsymbol{S}_2}{q}) \cdot \frac{\hat{\boldsymbol{L}}}{M^2} \tag{16}$$

and

$$\mathcal{S}_2 = 4 + \frac{3}{q} - \frac{3(1+q)^2}{q\sqrt{r/M}}(\boldsymbol{S}_1 + k_2\frac{\boldsymbol{S}_2}{q}) \cdot \frac{\hat{\boldsymbol{L}}}{M^2}\,, \tag{17}$$

as outlined by Ref [9]. In Equation 15, the $\frac{dL}{dt}$ term captures the loss of energy due to radiation reaction. Though, as discussed in Section II C, this has a negligible effect over one precessional cycle and can thus be set to 0 on $t_{\rm pre}$.

*With* our re-parameterization, Equations (13) - (15), and Equations 17-20 in Ref. [8], we can find the orbit-averaged evolution of $\chi_{\rm eff}$ and $\delta\chi$ to be,

$$M\frac{d\chi_{\rm eff}}{dt} = \frac{3}{4}\left(\frac{M}{r}\right)^{7/2}\frac{q\chi_1\chi_2}{(1+q)^2}[\chi_{\rm eff}(k_1-k_2) + \delta\chi(k_1+k_2-2)]\hat{\mathbf{L}}\cdot(\hat{\mathbf{S}}_{\mathbf{1}}\times\hat{\mathbf{S}}_{\mathbf{2}})\,, \tag{18}$$

$$M\frac{d\delta\chi}{dt} = -\frac{3}{4}\frac{M^3}{r^{7/2}}\frac{q\chi_1\chi_2}{(1+q)^2}\{-4\sqrt{r} + \sqrt{M}[\chi_{\rm eff}(2+k_1+k_2) + \delta\chi(k_1-k_2)]\}\mathbf{L}\cdot(\hat{\mathbf{S}}_{\mathbf{1}}\times\hat{\mathbf{S}}_{\mathbf{2}})\,. \tag{19}$$

Clearly in the BBH case, where $k_1 = k_2 = 1$, Equation (18) goes to 0, leaving Equation (19) to fully describe the spin dynamics up to $r > 10$. Thus, we are left with a much simpler problem.

In the BNS case $\chi_{\rm eff}$ is no longer constant on $t_{\rm pre}$; to find a new constant of motion we consider timescales such that radiation reaction is neglected, i.e. $dL/dt = 0$ in Equation 15. That means we restrict to $t \sim |d\hat{\mathbf{L}}/dt|^{-1} \ll L|dL/dt|$. Giulia Fumagalli finds that,

$$\frac{d}{dt}\left(\chi_{\rm eff} - \frac{\chi_{\rm eff}^2 + \chi_{\rm quad}^2}{2\sqrt{r/M}}\right) = 0, \tag{20}$$

where

$$\chi_{\rm quad}^2 \equiv \frac{1}{M^2}\left[(k_1-1)\left(\frac{\boldsymbol{S}_1\cdot\hat{\boldsymbol{L}}}{m_1}\right)^2 + (k_2-1)\left(\frac{\boldsymbol{S}_2\cdot\hat{\boldsymbol{L}}}{m_2}\right)^2\right] \tag{21}$$

$$= \frac{(k_1-1)(\chi_1\cos\theta_1)^2 + (k_2-1)(q\chi_2\cos\theta_2)^2}{(1+q)^2}\,.$$

Any function reliant on the term in the round brackets of Equation 20 is a constant of motion on $t_{\rm pre}$ with $dL/dt = 0$. We further require our desired conserved quantity to reduce to $\chi_{\rm eff}$ in both the BH limit $k_1 = k_2 = 1$ and the Newtonian limit $r \to \infty$. The resulting solution for a generalized conserved spin quantity is,

$$\chi_{\rm cons} = \frac{2\left(\chi_{\rm eff}^2 + \chi_{\rm quad}^2\right)}{1 + \sqrt{1 - \frac{2}{\sqrt{r/M}}\left(\chi_{\rm eff} - \frac{\chi_{\rm eff}^2+\chi_{\rm quad}^2}{2\sqrt{r/M}}\right)}}\,. \tag{22}$$

Thus, we are back to relying solely on Equation (19) to describe the evolution of our spins. While complex, Equations (19) and 22 are much simpler to handle than the 9-dimensional problem resulting from using Equations (13) - (15).

In summary, compact binaries in quasi-circular orbits are parameterized using $q, \chi_1, \chi_2, \chi_{\rm cons}, u, \kappa$, and $\delta\chi$. On $t_{\rm pre}$, since the effects of radiation reaction do not decrease (increase) the orbital separation $r$ (compactified coordinate $u$) significantly, we treat $u$ and $\kappa$ as constant. Also constant on $t_{\rm pre}$ is $q, \chi_1, \chi_2$, and $\chi_{\rm cons}$.

### F. Precession Averaging

To average a generic quantity $X$ over a precessional cycle

$$\tau_{\rm pre} = 2\int_{\delta\chi_-}^{\delta\chi_+}\left(\frac{d\delta\chi}{dt}\right)^{-1} d\delta\chi\,, \tag{23}$$

we perform the following calculation,

$$\langle X\rangle = \frac{\int_{\delta\chi_-}^{\delta\chi_+} X(\delta\chi)\left(\frac{d\delta\chi}{dt}\right)^{-1} d\delta\chi}{\tau_{\rm pre}}\,. \tag{24}$$

where $\delta\chi_-$ and $\delta\chi_+$ are the roots of Equation 19. For the generalized compact binary case, Equation 19 takes the form:

$$\left(\frac{d\delta\chi}{dt}\right)^2 = \mathcal{A}^2(1-\cos\theta_1)^2(1-\cos\theta_2)^2(1-\cos\Delta\Phi)^2\,. \tag{25}$$

where the four terms are defined as,

$$\mathcal{A} = \frac{3M^3 q\chi_1\chi_2\sqrt{\delta\chi^2 M(1-k_1k_2) - 2\sqrt{M}\sqrt{r}\left[\delta\chi(k_1-k_2)+\chi_{\rm cons}(k_1+k_2+2)\right] + M\chi^2_{\rm cons}(k_1+k_2+2)+4r}}{2(1+q)^2 r^{7/2}}\,, \tag{26}$$

$$\cos\theta_1 = \frac{(1+q)\left[2\sqrt{r/M}+(1+k_2)\delta\chi\right]}{(2+k_1+k_2)\chi_1} - \frac{(1+q)\sqrt{4r/M+(1-k_1k_2)\delta\chi^2+(2+k_1+k_2)\chi^2_{\rm cons}-2\sqrt{r}\left[(k_1-k_2)\delta\chi+(2+k_1+k_2)\chi_{\rm cons}\right]}}{(2+k_1+k_2)\chi_1}\,, \tag{27}$$

$$\cos\theta_2 = \frac{(1+q)\left[2\sqrt{r/M}-(1+k_1)\delta\chi\right]}{q(2+k_1+k_2)\chi_2} - \frac{(1+q)\sqrt{4r/M+(1-k_1k_2)\delta\chi^2+(2+k_1+k_2)\chi^2_{\rm cons}-2\sqrt{r}\left[(k_1-k_2)\delta\chi+(2+k_1+k_2)\chi_{\rm cons}\right]}}{q(2+k_1+k_2)\chi_2}\,, \tag{28}$$

and

$$\cos\Delta\Phi = \frac{2kq(q+1)^2\sqrt{r} - M^2\left[2q\chi_1\cos\theta_1\left(q\chi_2\sqrt{M}\cos\theta_2+\sqrt{r}\right)+2q^3\chi_2\sqrt{r}\cos\theta_2+\sqrt{M}\left(q^4\chi_2^2+\chi_1^2\right)\right]}{2M^{5/2}q^2\chi_1\chi_2\sin\theta_1\sin\theta_2}\,. \tag{29}$$

While analytical roots can be found for Equations (26) - (28), Equation (29) has no-analytical roots and thus finding the roots of Equation (25) requires interpolating across a grid of $\delta\chi$ values to obtain the roots. But, with precession averaging we can finally evolve our binaries on $t_{RR}$.

The important quantities that evolve on $t_{RR}$ are $u, \kappa$, and $\chi_{\rm cons}$. We can express the evolutions of $\kappa$ and $\chi_{\rm cons}$ as functions of $u$ and precession average their expressions,

$$\frac{d\kappa}{du} = \langle S^2\rangle\,, \tag{30}$$

where

$$S^2 = \frac{M^2}{u}\left[\frac{\kappa}{M^2} - \frac{(1+q)}{M^{3/2}qu(2+k_1+k_2)} - \frac{1+k_2-k_1(1+q)}{(1+q)(2+k_1+k_2)}\,\delta\chi + \frac{\sqrt{\mathcal{C}}}{Mqu(2+k_1+k_2)}\right] \tag{31}$$

and

$$\mathcal{C} = 1+q\Big\{(q+1)^2(q+4) - (q+1)^2M^{3/2}u\left[\chi_{\rm cons}(k_1+k_2+2)+\delta\chi(k_1-k_2)\right] + qM^3u^2\left[\chi^2_{\rm cons}(k_1+k_2+2)+\delta\chi^2(1-k_1k_2)\right]\Big\}.$$

Meanwhile,

$$\frac{d\chi_{\rm cons}}{{\rm d}u} = -\frac{(1+q)^2\left\{2+q\left[4+2q+u(k_2-k_1)\delta\chi-u(2+k_1+k_2)\chi_{\rm cons}\right]\right\}}{u^2q(2+k_1+k_2)\left[(1+q)^2-2qu\chi_{\rm cons}\right]} - \frac{(1+q)^2\left\{2\sqrt{(1+q)^4+q^2u^2[\delta\chi^2(1-k_1k_2)+\chi^2_{\rm cons}(2+k_1+k_2)]}-q(1+q)^2u[\delta\chi(k_1-k_2)+\chi_{\rm cons}(2+k_1+k_2)]\right\}}{u^2q(2+k_1+k_2)\left[(1+q)^2-2qu\chi_{\rm cons}\right]} \tag{32}$$

By integrating Equations (30) and (32) we can fully evolve BNSs. Due to the non-analytical form the roots

of Equation (25) take though, this integration – which requires precession averaging at each step of $u$ – is much slower (and not always accurate). We thus turn our focus to finding ways to make such calculations faster and accurate for all BNS configurations.

## III. APPROACH

In order to recreate the double-averaging approach that Gerosa *et al.* uses, and ultimately expand upon `Precession`, we take the following steps:

- *Fixing root-finding*: Starting from Giulia Fumagalli and Taylor Knapp's preliminary extension of the `Precession` code to BNSs, we have been investigating accurate and efficient ways to find the roots of $\frac{d\delta\chi}{dt}$. We do so by evaluating the roots of a cubic spline fit to the function, as there is no analytical solution for the roots. Refining this root-finding is necessary to precession average, as this requires finding one pair of roots which create a valid region to average over. We approach this by attempting to evolve a range of synthetic BNS scenarios and see where the code breaks down.

- *Optimizing*: With a robust way to evolve BNSs, we would like to speed up per-binary evolution times. Going into this project, a single binary would take over 10 seconds to evolve from $r = 1000$ to $r = 10$ at 100 steps of $r$, finding ways to speed this up is crucial for having a usable framework for further BNS inspiral study.

- *Investigating bifurcations*: The next challenge is that in higher $q$ and $k$ limits two sets of valid $\delta\chi$ roots are found defining separate, valid precessional cones to average over. This is not physically possible, but merely a result of the loss of phase information when precession averaging. Understanding how to approach this bifurcation case, or understanding which BNSs make precession averaging invalid, is crucial for a robust model for *all* possible NS binaries.

- *Testing and validation*: Afterwards, the code will be tested across a range of physical parameters, including masses, spin magnitudes, orbital separations, and NS equations of state. We will validate the implementation by comparing appropriate limits with known BH results.

- *Application to real events*: Finally, we will apply the developed framework to GW observations of NS binaries, with the goal of reconstructing their spin evolution and connecting measurable quantities, such as spin directions measured by LIGO, to their value at the formation of the binary.

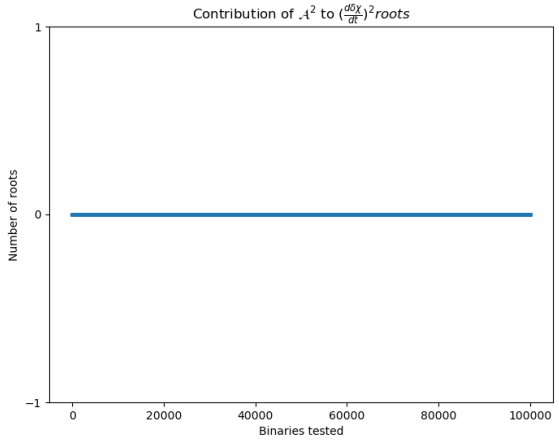



FIG. 4. The $\mathcal{A}^2$ roots at 100 steps of $r$ for 1000 binaries are found and in every binary, at every step (100,000 total points) $\mathcal{A}^2$ has no roots. Note that this is a scatter plot although it doesn't look it.

## IV. INTERIM PROGRESS AND RESULTS

### A. Removing $\mathcal{A}^2$ From Root-Finding

As brought up in Section III, we started off by looking for ways to make root-finding faster and robust in cases that do not lead to a bifurcation. To do so I started off by setting up 1000 initial BNS scenarios by sampling relevant quantities such as initial $\theta_1, \theta_2, \Delta\Phi, q, \chi_1, \chi_2, m_1,$ and $m_2$ from isotropic distributions. With these quantities, for each artificial binary I obtained $\kappa, \chi_{\rm cons}, k_1, k_2$ and $\delta\chi$. It is important to note that an APR equation of state was used to determine the maximum mass from which to sample, which also determined the used $k_1$ and $k_2$ values. I then found the roots of each term in Equation (25) to investigate the root-finding behavior. A particularly helpful finding was that the pre-factor $\mathcal{A}^2$ never contributed a physically meaningful root, thus there is no need to include it when evaluating the roots of Equation (25). This is nice as it reduces computational time. Figure 4 shows the number of roots from $\mathcal{A}^2$.

### B. New Root-Finding Bounds

Our next significant finding was the discovery of restrictive physical bounds on the grid for which we interpolate Equation (25). When trying to solve the issue of "spurious roots" mentioned in the first interim report I noticed a trend in every scenario I plotted, the roots of $\sin^2(\Delta\Phi)$ that weren't at discontinuities due to the other terms were always bounded by the roots of $\sin^2(\theta_1)$ and $\sin^2(\theta_2)$. Moreover, the positive part of the curve of $(\frac{d\delta\chi}{dt})^2$ was also within these bounds. We had not realized at first, but this behavior was clear in

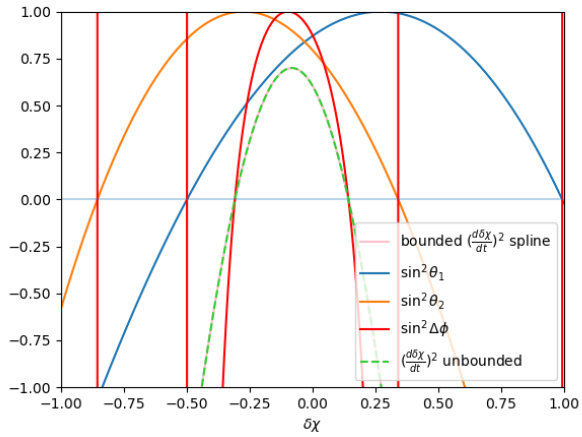



FIG. 5. Above are plots of the factors of Equation (25), Equation (25) itself, and the bounded spline of Equation (25) in the physical region described in Section IV B. As explained, $(\frac{d\delta\chi}{dt})^2$ is positive only in the region where each of its terms are also positive. As we would hope, the spline of $(\frac{d\delta\chi}{dt})^2$ overlaps nicely with its analytical form.

hindsight. Since we are finding the values of $\delta\chi$ where $(\frac{d\delta\chi}{dt})^2 = 0$, and $\delta\chi$ is a physical quantity, we need only consider the positive portion of $(\frac{d\delta\chi}{dt})^2$ in $\delta\chi \in [-1, 1]$. This, of course, occurs when each term of $(\frac{d\delta\chi}{dt})^2$ is positive. In Figure 5, the positive portion of $(\frac{d\delta\chi}{dt})^2$ is where each curve is positive. To apply this to our interpolation, we designed an algorithm to search for the first pair of roots from the analytical forms of $\sin^2\theta_1$ and $\sin^2\theta_2$ where the sorted pair's first root comes from a 'rising' curve and the second root comes from a 'falling' curve. This bounding of the interpolation grid made root-finding successful for a test of 1000 binary scenarios under the APR EOS.

Stepping out of chronological order, when testing the ability to evolve larger numbers of binaries – 10,000 binaries in particular – we found *one* case where the bound-finding logic failed. This was because it found a rising-falling pair of only $\sin^2\theta_1$ roots where $\sin^2\theta_2$ was actually negative. Thus, we implemented a check in the bound-finding algorithm that ensures at the midpoint on the $\delta\chi$ grid defined by the bounds found, all terms in Equation (25) are positive. If a term is not positive it checks the next rising-falling pair of roots.

### C. Evolution optimization

With a much more robust interpolation of Equation (25) we sought to decrease the time it took to evolve a binary. The first step we took to do this was optimize the grid for interpolation by finding the minimal number of points for which root-finding remains robust. This is quite sensitive and we have yet to find a good algorithmic way of doing this, especially since to evolve a large number of binaries across different grid sizes takes time on the order of days, but we find that 10,000 grid points is robust while not being much slower than 5,000 grid points (which caused some errors). By dropping the grid outside of the bounds we made interpolation even more efficient.

A simple next step to speed up evolution times was to wrap all algebraic functions with `NUMBA`'s NJIT decorator. At each r-step in the ODE solver of Equation (30) calls to each term of Equation (25) are made. The way this decorator works is it initially complies the decorated function into machine-language on the functions first call – essentially making execution of the function C-speed. Due to the large number of calls to the function describing Equation (25) this significantly improved evolution times.

On top of this decoration method, we noticed that terms within Equations (27) - (29) are repeated. By factoring such repeated terms out and calculating them once per r-step we further reduce evolution times.

Lastly, we found some binaries that failed to evolve due to internal issues from chosen ODE solver – `scipy.interpolate.solve_ivp`. After testing `scipy.interpolate.odeint`, used in Ref. [8], we found integration to be not only more robust, but also more efficient per-binary. Of note is that we did not fix the bound-finding logic before switching to `scipy.interpolate.odeint`, after fixing the bound-finding logic as described at the end of Section IV B we lost a little efficiency, but overall the robustness and speed of evolutions greatly increased compared to our original inspiral evolution times.

All of these implementations average per-binary evolution time for 50 binary evolutions is shown in 6 with the relative increase in speed compared to the code's speed at the start of the project.

### D. Bifurcations

With a much more robust and efficient way to evolve BNSs, we are able to investigate cases of BNS that bring about "bifurcations" in the spin evolution. These bifurcations are cases where the root-finder finds 4 roots at a given separation, unlike most cases which find 2 roots. This creates an issue because the ordered pairs of roots create two possible branches for which the spins could evolve into. This is not physical, for a given binary starting at some initial $\delta\chi$, orbit averaging of course finds a definite path for the binary's $\delta\chi$ to oscillate between. Thus, we hope to understand how to pick the correct branch when precession averaging.

This is of particular interest because these bifurcations

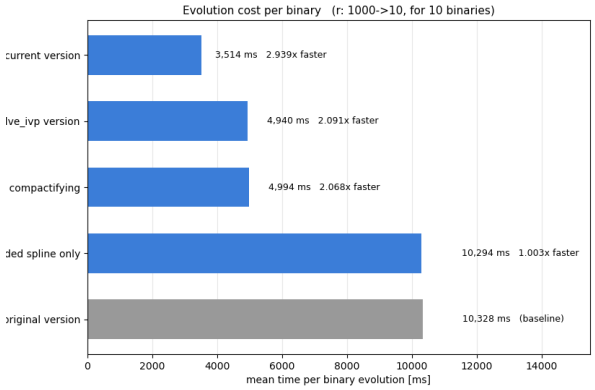



FIG. 6. A bar plot of the time (ms) it takes on average to evolve a binary using different adaptations of the code. *From bottom to top:* the oldest version of the code, the boundfinding approach implementation, the NJIT version, the NJIT version & compactified equation version, the current version used `scipy.interpolate.odeint`.

bring about noticeable changes in the morphology of the spin evolution, and generally seem to occur at higher values of $k$. Thus, it may be possible to verify, or rule-out, equations of state that admit high tidal deformabilities through the detection, or lack of detection, of binaries that when backwards evolved, show such changes in spin morphology. This bifurcation is shown in Figure 7.

To try and understand how to choose the correct branch when precession averaging, we looked at how starting at different $\delta\chi$ values affected orbit averaging. Such evolutions for the BNS configuration from Figure 7 are shown in Figure 8. Interestingly, there are evolutions that do not end up in either branch, and although the branch that evolutions end up in seems to be heavily influenced by initial $\delta\chi$, there isn't a clear distinction of initial $\delta\chi$ values that lead to a branch. We see most upper branch evolutions come from $\delta\chi < 0$ and most lower branch evolutions come from $\delta\chi > 0$, but this doesn't always hold. Thus, we need to look into such bifurcations further.

## V. CHALLENGES AND NEXT STEPS

The main challenge so far has been debugging root-finding along the way. Imposing the bounds on the spline helped but slowly revealed occasional errors that required further fixing, like the physicality check in root-finding and the switch of ODE solvers. Now, the big challenge, and where our next steps will be, is in understanding the bifurcations. While the presented bifurcation is symmetric, not all bifurcations are so nice and these require understanding as well. We will look further into how orbit-averaging handles bifurcations, with an initial focus on why some evolutions do not end up in a branch, and hopefully gain intuition on how to pick a valid branch for precession averaging.

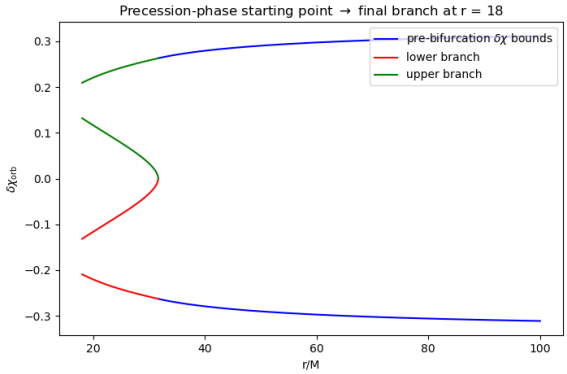



FIG. 7. A BNS with $q = \chi_1 = \chi_2 = 1$, $k_1 = k_2 = 10$, starting at $r = 10$, $\kappa = 0.364$ and $\chi_{\rm cons} = 0.539$ shows a bifurcation in the precession cone at $r = 31.63$.

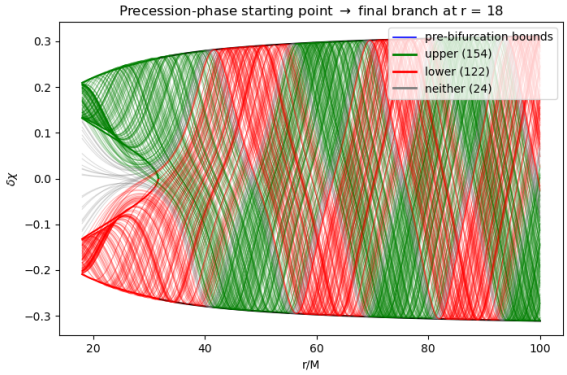



FIG. 8. The orbit averaged evolution of $\delta\chi$ for the binary in Figure 7, green evolutions end up in the upper branch, red ones end up in the lower branch, and gray ones fail to go into a branch. The number of evolutions that fall into each binary is displayed in the legend.


[1] T. A. Apostolatos, C. Cutler, G. J. Sussman, and K. S. Thorne, Spin-induced orbital precession and its modulation of the gravitational waveforms from merging binaries, Phys. Rev. D **49**, 6274 (1994).

[2] L. E. Kidder, Coalescing binary systems of compact objects to (post)$^{5/2}$-Newtonian order. V. Spin effects, Phys. Rev. D **52**, 821 (1995), arXiv:gr-qc/9506022 [gr-qc].

[3] É. Racine, Analysis of spin precession in binary black hole systems including quadrupole-monopole interaction,

Phys. Rev. D **78**, 044021 (2008), arXiv:0803.1820 [gr-qc].
[4] D. Gerosa, M. Kesden, U. Sperhake, E. Berti, and R. O'Shaughnessy, Multi-timescale analysis of phase transitions in precessing black-hole binaries, Phys. Rev. D **92**, 064016 (2015), arXiv:1506.03492 [gr-qc].
[5] A. Einstein and N. Rosen, On gravitational waves, Journal of the Franklin Institute **223**, 43 (1937).
[6] B. P. e. a. Abbott (LIGO Scientific Collaboration and Virgo Collaboration), Observation of gravitational waves from a binary black hole merger, Phys. Rev. Lett. **116**, 061102 (2016).
[7] C. L. Rodriguez, M. Zevin, C. Pankow, V. Kalogera, and F. A. Rasio, Illuminating Black Hole Binary Formation Channels with Spins in Advanced LIGO, Astrophys. J. Lett. **832**, L2 (2016), arXiv:1609.05916 [astro-ph.HE].
[8] D. Gerosa, G. Fumagalli, M. Mould, G. Cavallotto, D. P. Monroy, D. Gangardt, and V. De Renzis, Efficient multi-timescale dynamics of precessing black-hole binaries, Phys. Rev. D **108**, 024042 (2023), arXiv:2304.04801 [gr-qc].
[9] A. Klein, Efpe: Efficient fully precessing eccentric gravitational waveforms for binaries with long inspirals (2021), arXiv:2106.10291 [gr-qc].
[10] D. Gerosa, U. Sperhake, and J. Vošmera, On the equal-mass limit of precessing black-hole binaries, Classical and Quantum Gravity **34**, 064004 (2017).